



Fatigue deformation mechanism of the Mg–Nd alloys

Peng Zhang¹ and Zhenming Li^{2,3,*}

¹ Shanghai Automobile Gear Works, Central Laboratory, Shanghai 201807, People's Republic of China

² Zhejiang Jinyue Machinery Technology Development Co. Ltd, Jinhua 330096, People's Republic of China

³ Automobile and Motorcycle Parts Research Academy Technology Co. Ltd, Zhejiang Jinfei Kaida Wheel Co. LTD, Jinhua 330096, People's Republic of China

Received: 17 September 2022

Accepted: 4 December 2022

Published online:

1 January 2023

© The Author(s), under exclusive licence to Springer Science+Business Media, LLC, part of Springer Nature 2022

ABSTRACT

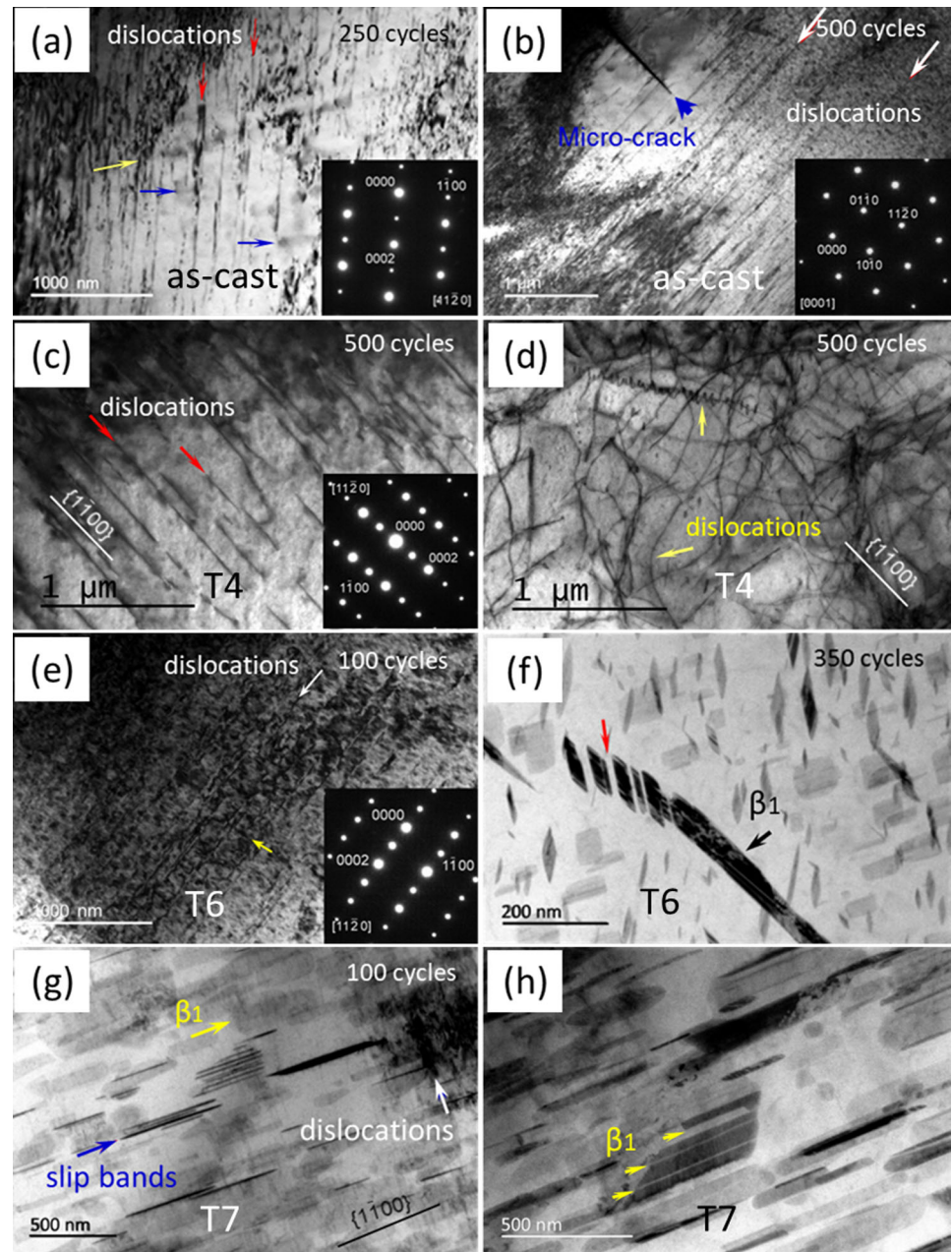
Low cycle fatigue behavior of the Mg–3.68 wt%Nd–0.58 wt%Zr alloy was investigated in both as-cast and various heat-treated conditions and the T6-treated (peak-aged) Mg–3.69 wt%Nd alloy in terms of cyclic stress responses with microstructure evolution. Dislocation-slip mechanism was found to be responsible for the fatigue deformation in the grain-refined material in both the as-cast and the T4-treated (solution) conditions and in the non-grain-refined material in the T6-treated condition. Dislocation interaction with precipitates and twins dominating cyclic deformation was only observed in the grain-refined material with aging hardening conditions. The constant stress amplitudes observed in the as-cast and the T7-treated (over-aged) conditions in the grain-refined material are attributed to the competing mechanism of work hardening and stress release caused by the cracks and slip bands, respectively. The transformation of precipitates from β'' to β_1 and β and the coarsening of β_1 precipitate leads to the cyclic softening in the T6-treated alloy. The shearing mechanism of dislocations is the main reason for the change of precipitate in the alloy.

Handling Editor: P. Nash.

Address correspondence to E-mail: lizhenming516@163.com

<https://doi.org/10.1007/s10853-022-08060-4>

GRAPHICAL ABSTRACT



Introduction

Heat treatment changes the microstructure of the magnesium alloys, thus affecting their fatigue properties [1–8]. It has been reported that the cyclic stress

response behavior of the Mg–3Nd–0.2Zn–1Zr (NZ30K) alloy under as-cast and heat treatment conditions is obviously different during low cycle fatigue process [9, 10]. At the total strain amplitude of 0.4%, the stress amplitude of the as-cast alloy increases in the initial cyclic loading stage (below

about 100 cycles) and then remains unchanged until failure, showing initial cyclic hardening followed by cyclic saturation. For the T4-treated alloy (solution heat treated condition: 540 °C × 10 h), the stress amplitude increases with the increase of number of cycles. The trend of the initial work hardening is slow, and after 100 cycles the hardening is accelerated obviously. Overall, the T4-treated alloy shows obvious work hardening trend throughout the entire fatigue testing. The precipitates in the T6-treated (peak-aged treatment, 540 °C × 10 h + 200 °C × 14 h) and the T7-treated (over-aged treatment, 540 °C × 10 h + 250 °C × 10 h) alloys are finer β'' precipitates (Mg_3Nd , hcp, D0_{19} , $a = 0.64$ nm, $c = 0.52$ nm, hexagonal prism) [11] and relatively coarser β_1 precipitates (Mg_3Nd , fcc, $a = 0.74$ nm, $\{10\text{--}10\}_\alpha$ plate) [12], respectively. The stress amplitude of the T6-treated alloy is increased in the beginning of cyclic loading. After certain number of cycles (say ~ 350 cycles), the stress amplitude of the alloy decreases. Generally, the T6-treated alloy shows a trend of initial hardening and then softening [13]. In contrast, the T7-treated alloy shows neither hardening nor softening with the increase of the number of cycles. In addition, for an extruded Mg–3Nd–0.2Zn–0.5Zr magnesium alloy [14], cyclic softening occurs at lower strain amplitudes while cyclic hardening occurs at higher strain amplitudes. Wang et al. [15] pointed out that an extruded Mg–8.0Gd–3.0Y–0.5Zr magnesium alloy shows nearly symmetrical stress–strain hysteresis loops and marginal cyclic hardening, and the mean stress is almost zero during low cycle fatigue. This is similar to the findings reported for an extruded Mg–10Gd–2Y–0.5Zr alloy [16], where tension–compression yield symmetry was observed. Moreover, Yin et al. [17] also suggested that at strain amplitudes of 0.2% to 1%, the extruded Mg–12%Gd–3%Y–0.5Zr alloy kept the cyclic stability prior to fatigue failure. For an extruded Mg–8Al–0.5Zn alloy [4], an abrupt increase in the plastic strain amplitude shows the onset of the fatigue crack initiation on the surface of the fatigue samples.

The cyclic deformation behavior of a metallic alloy is mainly dependent on the characteristics of dislocation movement and microstructure evolution [18–21]. For the Mg–Nd-based alloy during fatigue, however, there are few in-depth studies on the influence of heat treatment and grain size on microstructure evolution, especially on the interaction mechanism between dislocations and second

phase particles, precipitates and twins [22–25]. It is important to understand the relationship between the existing forms of Nd element, grain size and deformation mechanism for the structure optimization and practical application of the Mg alloys containing Nd. In the present study, the as-cast and the heat-treated (T4, T6 and T7) Mg–3.68 wt%Nd–0.58 wt%Zr alloy (actual chemical composition) materials and the T6-treated Mg–3.69 wt%Nd were tested at strain amplitudes of 0.2% and 0.4% for certain numbers of cycles, respectively. TEM analyses were conducted on the fatigued samples to explore the microstructure evolution of the Mg–3.68 wt%Nd–0.58 wt%Zr alloy from as-cast to various heat treatment conditions (solution heat treated T4, peak-aged T6 and over-aged T7) and the T6-treated Mg–3.69 wt%Nd alloy during the low cycle fatigue.

Experimental procedure

In this work, the materials are the Mg–3.68 wt%Nd–0.58 wt%Zr alloy (average grain size of $\sim 51 \pm 5$ μm) and the Mg–3.69 wt%Nd alloy (average grain size of $\sim 1625 \pm 236$ μm) the prepared by gravity permanent mold casting process. The casting process in the present study is the same as that reported in [26]. The heat treatment of the alloy consists of solution treated at 550 °C for 8 h (T4), and then either peak-aged at 200 °C for 10 h (T6) or over-aged at 200 °C for 120 h (T7), respectively.

The tensile samples (gage dimensions of ϕ 6 mm × 30 mm) were tested on an Instron tensile machine at room temperature and a crosshead speed of 1 mm/min. Three tensile specimens were tested and the average tensile properties were reported. The fatigue samples (gage dimensions of ϕ 6.25 mm × 12.5 mm) were performed on Instron fatigue machine using the strain-controlled mode (triangular waveform $R = -1$, frequency of 1 Hz). At the strain amplitude of 0.4%, the fatigue tests of the Mg–3.68 wt%Nd–0.58 wt%Zr alloy under the as-cast and the heat treatment conditions were terminated after certain numbers of cycles (100 cycles (T6 and T7), 250 cycles (as-cast), 350 cycles (T6), 500 cycles (as-cast and T4), and 1000 cycles (T6 and T7)). At the strain amplitude of 0.2%, however, the fatigue testing was performed until 10^4 cycles for both the T4- and the T6-treated Mg–3.68 wt%Nd–0.58 wt%Zr alloy. In addition, for the T6-treated Mg–3.69 wt%Nd alloy,

the tests were interrupted after 200 cycles (hardening stage), 500 cycles (peak stress point) and 1000 cycles (softening stage), respectively. The dislocation structure in the fatigue-tested specimens was observed under TEM. The dislocation morphology and microstructure evolution of the fatigue-tested samples were observed using JEM-2100 TEM and FEI TECNAI G2 20 high-resolution projection electron microscope. TEM specimens were electropolished by double spraying at temperature of $-25\text{ }^{\circ}\text{C}$, electrical current of 0.2 A and working voltage of 45 V.

Results and discussion

Microstructure and tensile properties

Figure 1 shows the typical microstructure characteristics of the eutectic particles and the precipitates within the grains of the Mg–3.68 wt%Nd–0.58 wt%Zr alloy under the as-cast and the heat treatment conditions (T6 and T7). Similar to NZ30K (Mg–3Nd–0.2Zn–1Zr) alloy [11], the microstructure of the as-cast Mg–3.68 wt%Nd–0.58 wt%Zr alloy mainly consists of α -Mg matrix and hard β_e -Mg₄₁Nd₅ eutectic particles (tetragonal, $I41m$, $a = 1.47\text{ nm}$, $c = 1.04\text{ nm}$) (on $\{1-100\}_\alpha$ and $\{11-20\}_\alpha$ planes) [12] (as shown in Fig. 1a), while the T4-treated alloy merely consists of a supersaturated solid solution and α -Mg matrix [11]. For the T6-treated alloy (as shown in Fig. 1b), the fine

β'' precipitates (on $\{1-100\}_\alpha$ and $\{11-20\}_\alpha$ planes) have a completely coherent relationship with the matrix, resulting in a lattice distortion and effectively blocking dislocation movement to achieve the purpose of strengthening [11, 12]. In contrast, the large precipitates (length of 200–1000 nm, width of 50–500 nm) in the T7-treated Mg–3.68 wt%Nd–0.58 wt%Zr alloy are considered as β_1 precipitates on $\{1-100\}_\alpha$ and $\{11-20\}_\alpha$ planes (marked by yellow arrow in Fig. 1c) [12]. As shown in Fig. 1d, the microstructure of the coarse-grained Mg–3.69 wt% alloy before fatigue testing mainly consists of large number of fine β'' precipitates (marked by the yellow arrow) and a small amount of large β_1 precipitates (marked by the red arrow).

The tensile properties of the Mg–3.68 wt%Nd–0.58 wt%Zr alloy under the as-cast and the heat treatment conditions and the T6-treated Mg–3.69 wt% alloy are summarized in Table 1. The yield strength (YS) and ultimate tensile strength (UTS) of the Mg–3.68 wt%Nd–0.58 wt%Zr alloy slightly decrease after solution treatment (T4). In contrast, the ductility of the alloy is significantly improved (from 7.9 to 15.3%). After ageing treatment, the YS and UTS of the alloy are significantly increased from about 83 MPa (T4) to 156 MPa (T6) or 145 MPa (T7) and about 192 MPa (T4) to 283 MPa (T6) or 271 MPa (T7), while the elongation is remarkably decreased from about 15.3% (T4) to 6.8% (T6) or 11.5% (T7).

Figure 1 Bright field images showing the phases and precipitates in the pre-fatigue Mg–3.68 wt%Nd–0.58 wt%Zr alloy under **a** as-cast; **b** T6-treated condition; and **c** T7-treated condition ($B = [0001]_\alpha$). **d** Bright field image showing the precipitates of the T6-treated Mg–3.69 wt%Nd alloy with coarse-grains before fatigue testing ($B = [11-20]_\alpha$).

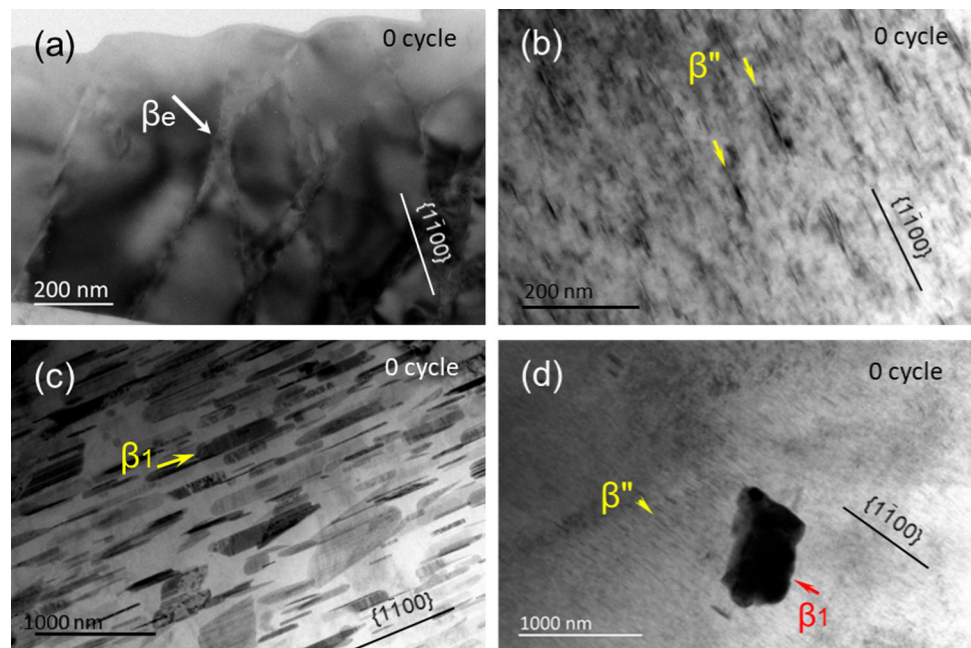


Table 1 Tensile properties of the Mg–3.68Nd–0.58Zr alloy under as-cast and heat treatment conditions

Alloys	Heat treatments	YS (MPa)	UTS (MPa)	Elongation (pct)
Mg–3.68 wt%Nd–0.58 wt%Zr alloy	as-cast	94 ± 2.1	203 ± 4.7	7.9 ± 2.3
	T4-treated	83 ± 3.6	192 ± 2.8	15.3 ± 1.4
	T6-treated	156 ± 3.7	283 ± 3.4	6.8 ± 1.2
	T7-treated	145 ± 1.8	271 ± 2.5	11.5 ± 1.5
Mg–3.69 wt%Nd alloy	T6-treated	49 ± 5.7	112 ± 4.8	4.6 ± 2.1

Compared with the T6-treated Mg–3.68 wt%Nd–0.58 wt%Zr alloy with fine grains, the T6-treated Mg–3.69 wt% without Zr addition exhibits lower tensile strengths (YS of 49 MPa, UTS of 112 MPa) and elongation (about 4.6%) due to large grains.

Cyclic stress response behavior

Figure 2 shows the variation of the cyclic stress amplitude for the as-cast and the heat-treated Mg–3.68 wt%Nd–0.58 wt%Zr alloy tested at the strain amplitudes of 0.2 and 0.4%. Moreover, the curve of the T6-treated Mg–3.69 wt%Nd alloy tested at the total strain amplitude of 0.4% is also included for comparison. Initial cyclic stress amplitude (σ_0 , 1th cycle), maximum stress amplitude (σ_{Max}), and $\Delta\sigma$ ($= \sigma_{Max} - \sigma_0$) of the Mg–Nd alloys tested at total

strain amplitude of 0.2% and 0.4% are summarized in Table 2. Similar to the NZ30K alloys [9], the stress amplitude of the as-cast Mg–3.68 wt%Nd–0.58 wt%Zr alloy initially increases and then remains saturated during the entire low cycle fatigue, while the stress amplitude of the T4-treated alloy is continuously increased until failure. The T4-treated alloy exhibits lower initial stress amplitude ($\sigma_0 = 79$ MPa) and higher cyclic hardening rate ($\Delta\sigma = 34$ MPa) in comparison with the as-cast alloy ($\sigma_0 = 91$ MPa and $\Delta\sigma = 19$ MPa), which is generally attributed to the influence of Mg–Nd eutectic particles. For the T7-treated alloy, the stress amplitude keeps almost constant at the strain amplitude of 0.4% ($\Delta\sigma = 4$ MPa). The stress amplitude of the T6-treated alloy first increases ($\Delta\sigma = 24$ MPa) and then decreases until failure. Furthermore, compared with the T7-treated alloy, the T6-treated alloy has higher cyclic stress amplitude (+ 35 MPa) due to higher yield strength (+ 11 MPa). The difference in cyclic response behavior between the peak-aged and the over-aged alloy is mainly attributed to the different types of the precipitates present (matrix-coherent β'' and matrix-incoherent β_1 precipitates) (as shown in Fig. 1) [12].

At the total strain amplitude of 0.2% (as shown in Fig. 2), the peak-aged (T6-treated) Mg–3.68 wt%Nd–0.58 wt%Zr alloy shows higher initial stress amplitude ($\sigma_0 = 90$ MPa) than that for the solid-solutionized (T4) alloy ($\sigma_0 = 55$ MPa) due to the higher yield strength (+ 73 MPa). In addition, the stress amplitude of the T6-treated alloy keeps constant while the stress amplitude of the T4-treated counterpart is increased after 500 cycles during fatigue process. It is seen from Fig. 2 that the T6-treated alloy exhibits the characteristics of cyclic hardening first and then cyclic softening (at total strain amplitude of 0.4%). The inflection point of cyclic stress amplitude of the T6-treated alloys generally occurs at about 350–450 cycles. After reaching to the peak stress point, the cyclic stress amplitude of the coarse-grained alloy

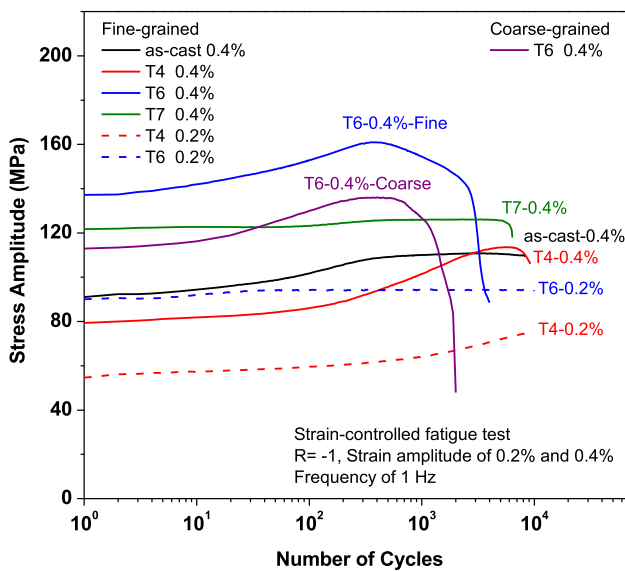


Figure 2 Variation of cyclic stress amplitude with the number of cycles for the as-cast, T4-, T6- and the T7-treated Mg–3.68 wt%Nd–0.58 wt%Zr alloy with fine-grains and the T6-treated Mg–3.69 wt%Nd alloy with coarse-grains tested at the total strain amplitude of 0.4%. The curves of the T4- and the T6-treated Mg–3.68 wt%Nd–0.58 wt%Zr alloys tested at the total strain amplitude of 0.2% are also included for comparison.

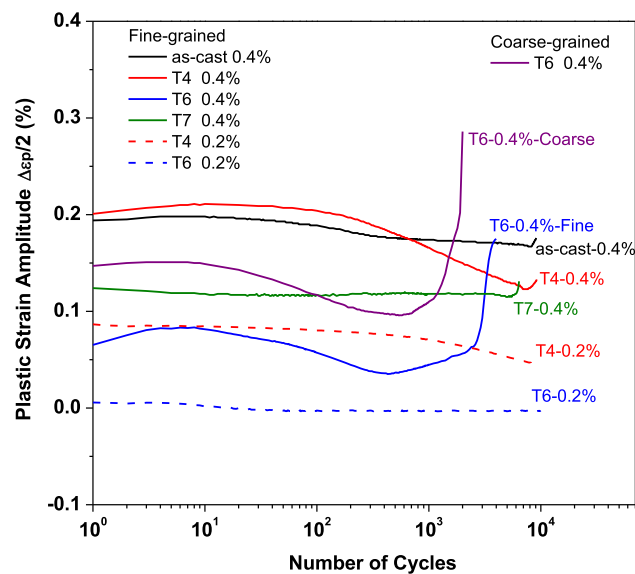
Table 2 Initial cyclic stress amplitude (σ_0), maximum stress amplitude (σ_{Max}), and $\Delta\sigma$ ($=\sigma_{\text{Max}} - \sigma_0$) of the Mg–3.68 wt%Nd–0.58 wt%Zr alloy and the T6-treated Mg–3.69 wt%Nd tested at the total strain amplitudes of 0.2% and 0.4%

Alloys	Heat treatments	Initial cyclic stress amplitude σ_0 (MPa)	Maximum stress amplitude σ_{Max} (MPa)	$\Delta\sigma = \sigma_{\text{Max}} - \sigma_0$ (MPa)
Mg–3.68 wt%Nd–0.58 wt%Zr alloy, 0.4%	as-cast	91	110	19
	T4-treated	79	113	34
	T6-treated	137	161	24
	T7-treated	122	126	4
Mg–3.68 wt%Nd–0.58 wt%Zr alloy, 0.2%	T4-treated	55	75	20
	T6-treated	90	94	4
Mg–3.69 wt%Nd alloy, 0.4%	T6-treated	113	136	23

presents a sudden decline trend, while the stress amplitude of the fine-grained alloy decreases relatively slowly. In contrast, the T6-treated alloys with different grains exhibit the same value of $\Delta\sigma$ (about 23–24 MPa).

Cyclic strain resistance

The relationship between the plastic strain amplitude and the number of cycles for the Mg–3.68 wt%Nd–0.58 wt%Zr alloy under the as-cast and the heat treatment conditions is shown in Fig. 3. At the total strain amplitude of 0.4%, the plastic strain

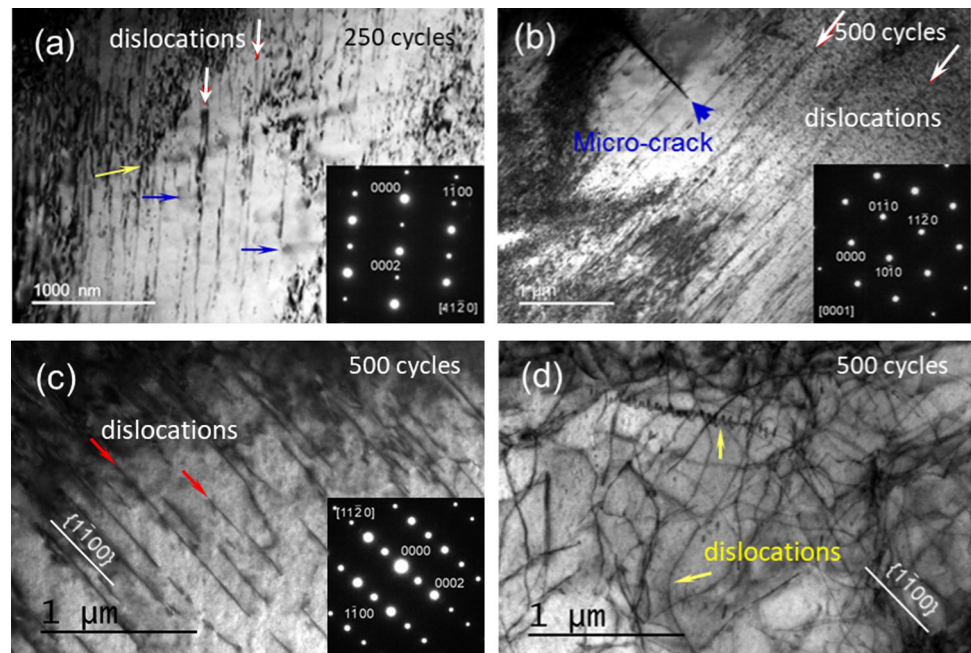
**Figure 3** Variation of plastic strain amplitudes with the number of cycles for the as-cast, T4-, T6- and T7-treated Mg–3.68 wt%Nd–0.58 wt%Zr alloy tested at the total strain amplitude of 0.2% and 0.4%. The curve of the T6-treated Mg–3.69 wt%Nd alloy tested at the total strain amplitude of 0.4% is also included for comparison.

amplitudes of the as-cast and the T4-treated alloy are decreased during the low cycle fatigue testing. For the T7-treated alloy, the plastic strain amplitude remains nearly unchanged before final failure. In contrast, the plastic strain amplitude of the T6-treated alloy decreases in the initial cyclic loading stage, and then increases until failure during fatigue. At the total strain amplitude of 0.2%, the plastic strain amplitude of the T6-treated alloy is near zero, while that of the T4-treated alloy decreases with the increase of number of cycles. The curve of the T6-treated Mg–3.69 wt% alloy is also included in Fig. 3 for comparison. For the plastic strain amplitude, as shown in Fig. 3, the coarse-grained alloy shows a similar change as the fine-grained alloy tested at the same strain amplitude.

Effect of eutectic particles

Figure 4 shows the typical dislocation distribution and the corresponding diffraction spots of the as-cast and the T4-treated Mg–3.68 wt%Nd–0.58 wt%Zr alloy after 250 and 500 cycles, respectively. The electron beam is nearly parallel to the Mg matrix $(11-20)_\alpha$ and $[0001]_\alpha$, respectively. Under the condition of $g = 1-100$, a large number of the dislocations were observed at the $\{1-100\}_\alpha$ prism plane for the as-cast alloy after 250 cycles (marked by red arrows in Fig. 4a). Moreover, a small amount of the dislocations at the $\{11-20\}_\alpha$ and $\{0001\}_\alpha$ can also be found (marked by yellow and blue arrows in Fig. 4a). On the whole, the dislocations of the as-cast alloy are dominated by straight dislocation slip bands. After 500 cycles, in addition to the high density dislocations (marked by white arrows in Fig. 4b), a few of microcracks (length of 50–100 nm) were formed in the as-cast alloy

Figure 4 **a** Bright field image of the as-cast Mg–3.68 wt%Nd–0.58 wt%Zr alloy tested at a strain amplitude of 0.4% after 250 cycles ($B = [11\text{--}20]_{\alpha}$); **b** bright field image showing the micro-cracks in the as-cast alloy after 500 cycles ($B = [0001]_{\alpha}$). **c** bright field image of the T4-treated Mg–3.68 wt%Nd–0.58 wt%Zr alloy tested at a strain amplitude of 0.4% after 500 cycles ($B = [11\text{--}20]_{\alpha}$); **d** bright field image showing another typical dislocation morphology in the T4-treated alloy ($B = [11\text{--}20]_{\alpha}$).



(marked by blue arrows in Fig. 4b). The cracks originated mainly from the cracked slip bands on the $\{11\text{--}20\}_{\alpha}$ and $\{1\text{--}100\}_{\alpha}$ planes. Crack initiation is due to the localization or accumulated deformation during fatigue, which is closely related to dislocation motion behavior [27–30].

As shown in Fig. 4c, there are a large number of dislocation slip bands (marked by red arrows) in the matrix of the T4-treated Mg–3.68 wt%Nd–0.58 wt%Zr alloy after 500 cycles. Similar to the as-cast alloy, most of the dislocations are mainly located at the $\{1\text{--}100\}_{\alpha}$ prism plane. Moreover, another type of dislocations with different configurations can be also observed in the matrix of the T4-treated alloy (marked by yellow arrows in Fig. 4d). The dislocations are mainly composed of short straight dislocations and curved dislocations located on the $\{1\text{--}100\}$ and $\{11\text{--}20\}$ planes. Similar curved dislocations were also formed in the N30K-T4 and NZ30K-T4 alloys after tensile deformation [31]. Compared with the as-cast alloy, a large number of the curved dislocations are seen in the T4-treated alloy. There is no evidence of twinning in plastic deformation during the low cycle fatigue process. On the whole, cyclic deformation behavior of the as-cast and the T4-treated Mg–3.68 wt%Nd–0.58 wt%Zr alloy is mainly dominated by dislocations-slip.

For the as-cast alloy, the cyclic hardening at the early stage of fatigue is mainly due to the formation

of a large number of dislocations and the interaction between the dislocations and grain boundaries and Mg–Nd eutectic particles. After solid solution treatment (T4), the yield strength of the alloy is slightly decreased (by ~ 10 MPa) in comparison with the as-cast alloy. For the T4-treated alloy, only the grain boundary hinders the dislocation movement during fatigue because the eutectic compounds almost fully dissolve into the matrix. With the increase of the number of cycles, in the region with low dislocation density, the matrix continuously deforms and forms dislocation entanglement, resulting in cyclic hardening until failure. After 500 cycles, the cyclic stress response of the as-cast alloy keeps cyclic stabilization, which is the result of the competing mechanisms of micro-hardening and micro-softening. During the low cycle fatigue process, there is an equilibrium relationship between the hardening caused by dislocation entanglement and the stress release from micro-crack initiation.

Effect of matrix strength

The microstructure of the T4-treated alloy merely consists of α -Mg matrix which is a highly supersaturated solid solution. The strain-hardening occurs mainly due to solid solution strengthening and grain boundary strengthening. For the T6-treated alloy with the fine β'' precipitates, cyclic response is mainly dependent on the precipitates and the grain

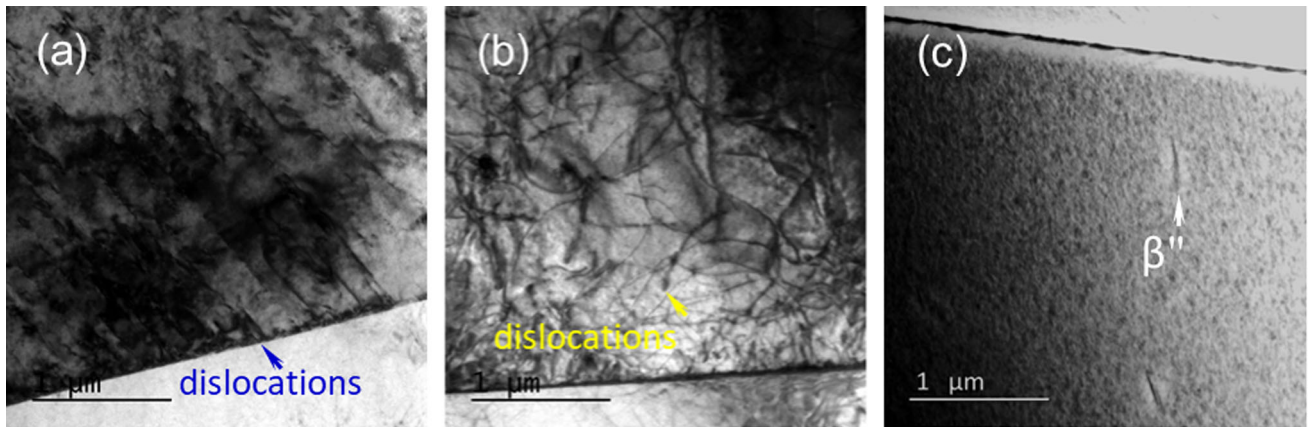


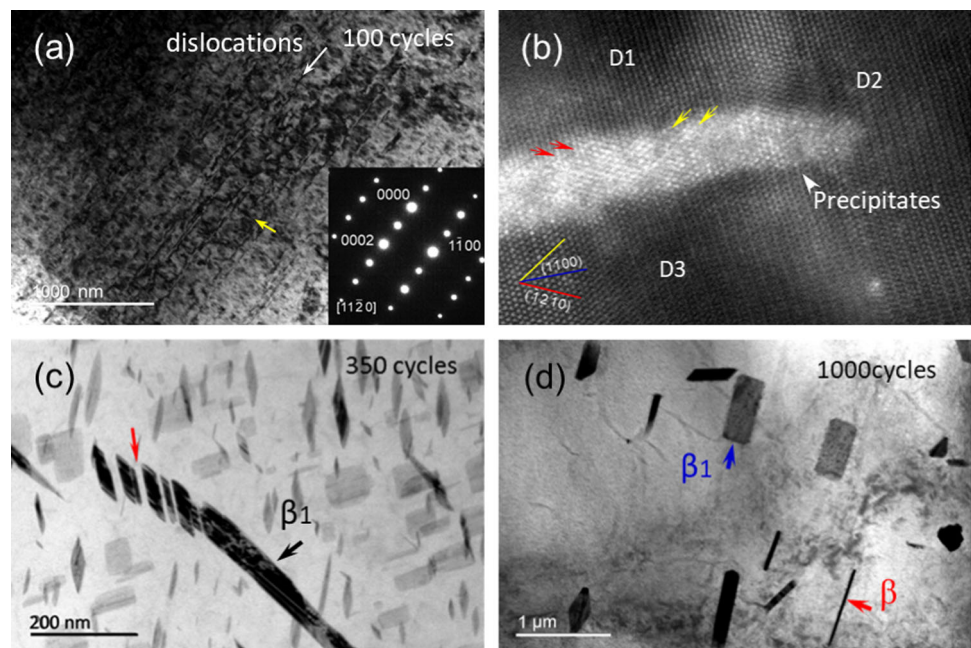
Figure 5 Bright field images of (a and b) the T4-treated and c the T6-treated Mg–3.68 wt%Nd–0.58 wt%Zr alloy tested at a strain amplitude of 0.2% after 10,000 cycles ($B = [11\bar{2}0]_a$).

boundaries. **Figure 5** shows the typical structures of the dislocations observed in the T4- and T6-treated Mg–3.68Nd–0.58Zr alloy at the strain amplitude of 0.2% after 10,000 cycles. It can be seen that a large number of the straight dislocations (marked by blue arrow in Fig. 5a) and curved dislocations (marked by yellow arrow in Fig. 5b) were formed in the matrix of the T4-treated alloy after 10,000 cycles. In contrast, except for the fine β'' precipitates (marked by white arrow in Fig. 5c), there is almost no dislocation in the T6-treated alloy after 10,000 cycles. As the T4-treated alloy has lower matrix strengths than the T6-treated counterpart, the T4-treated matrix can deform at the strain amplitude of 0.2% and then form high-density

dislocations entanglement, resulting in cyclic micro-hardening and finally working hardening.

Figure 6 shows the typical morphology of the precipitates and the dislocations in the T6-treated Mg–3.68 wt%Nd–0.58 wt%Zr alloy tested at the total strain amplitude of 0.4% after 100 cycles (hardening stage), 350 cycles (peak stress point) and 1000 cycles (softening stage). The typical dislocation distribution of the T6-treated alloy after 100 cycles (stress increasing stage) is shown in Fig. 6a ($B = [11\bar{2}0]_a$). There are many dislocations (marked by white and yellow arrows) within the grains and near the grain boundary. Similar to the T4-treated alloy, the dislocations of the T6-treated counterpart are also mainly

Figure 6 a Bright field image showing the typical distribution of the dislocations of the T6-treated Mg–3.68Nd–0.58Zr alloy tested at strain amplitude of 0.4% after 100 cycles ($B = [11\bar{2}0]_a$); b High-resolution dark field images showing the precipitates and dislocations (marked as D_{1-3}) near the precipitates; c Bright field image showing the β_1 precipitates were cut by dislocations in the T6-treated alloy after 350 cycles; d Bright field image showing the β_1 and β precipitates in the T6-treated alloy after 1000 cycles.



located at $\{1-100\}_\alpha$ prism planes. High-resolution dark field image in Fig. 6b shows that the β'' precipitates (marked by white arrow) and the dislocations near the precipitates in the T6-treated alloy after 100 cycles ($B = [0001]_\alpha$). It can be seen that the movement of the dislocations (marked as D_{1-3}) was blocked by the precipitates. As the precipitates in the T6-treated alloy are metastable β'' precipitates, they are easy to be sheared repeatedly by the dislocations during fatigue. It is believed that the dislocations cut from the surface of the precipitates (marked by red and yellow arrows). The phenomenon of the dislocations cutting through the precipitates mainly occurs at the $\{11-20\}_\alpha$ prism plane. Our previous research reported in detail the interaction mechanism between the dislocations, precipitates and twins of the T6-treated Mg-3Nd-0.2Zn-1Zr alloy [32]. At room temperature, the cyclic softening for the T6-treated alloy is mainly attributed to the shearing of the dislocations through the precipitates and the transformation of the precipitates [33–36].

After 350 cycles (peak cyclic stress amplitude point) of the T6-treated alloy, the type and size of the precipitates have changed obviously (as shown in Fig. 6c), from fine β'' precipitates to larger β_1 precipitates [12, 32]. Moreover, a small amount of band-shaped β_1 precipitates can be observed in the T6-treated alloy. The β_1 precipitates have been also cut by dislocations in the T6-treated alloy after 350 cycles. After 1000 cycles (cyclic stress amplitude decreasing stage), there are some massive β_1 precipitates and needle-like β precipitates (Mg_{12}Nd , tetragonal, $a = 1.03$ nm and $c = 0.59$ nm) [12] formed in the T6-treated alloy (as shown in Fig. 6d). For the T6-treated alloy, the change of the cyclic stress amplitude shows a trend of initial hardening followed by softening, corresponding to the transformation of the precipitates. At cyclic hardening stage, the β'' precipitates gradually change to the β_1 precipitates. The initial hardening is mainly attributed to the barrier of β'' precipitates and β_1 precipitates to the dislocations and dislocation entanglement. Cyclic softening is due to the micro-softening caused by phase transformation (from β'' precipitates and β_1 precipitates (marked by blue arrows) to β precipitates (marked by red arrows)) [32, 37–39].

As shown in Fig. 7a, persistent slip bands (PSBs) are formed in the matrix of the T6-treated Mg-3.68Nd-0.58Zr alloy after 350 cycles. The PSBs located at the $\{1-100\}_\alpha$ prism planes are thin and straight,

indicating the characteristics of the dislocations cutting precipitates multiple times [40–42]. During low cycle fatigue process, deformation behavior of the T6-treated alloy tends to experience three development stages, including dislocation-slip in the matrix, micro persistent slip lines, initiation and propagation of the PSBs. In addition, the twins also participate in the cyclic deformation of the T6-treated alloy after 350 cycles (as shown in Fig. 7b) [32]. For the magnesium alloys, both dislocations-slip and $\{10-12\}$ twinning are the main plastic deformation modes [43–45]. In our previous paper [32], the role and characteristics of the twinning in the NZ30K-T6 alloy during low cycle fatigue process were studied in detail.

The configuration of the typical dislocations and slip bands in the T7-treated alloy tested at the total strain amplitude of 0.4% for 100 cycles is shown in Fig. 8a. The dislocations in the T7-treated alloy are composed of dislocation slip bands located at $\{0001\}_\alpha$ plane and $\{1-100\}_\alpha$ prism plane. It can be seen that the slip bands (marked by blue arrow) at the $\{1-100\}_\alpha$ plane are fine and straight (length of 80–700 nm, width of 5–50 nm). The slip bands in the matrix of the T7-treated alloy have the PSBs structure [46, 47]. After 1000 cycles, the microstructure of the T7-treated alloy is almost the same as that of the counterpart after 100 cycles (as shown in Fig. 8b).

Similar to the T6-treated alloy, the β_1 precipitates in the matrix of the T7-treated counterpart were cut by the dislocations (marked by yellow arrows in Fig. 8c). The microstructure of the T7-treated alloy mainly consists of the β_1 precipitates, the dislocations and slip bands on $\{1-100\}$ prism plane during low fatigue process. For the T7-treated alloy, the stabilization of the cyclic stress amplitude is mainly due to the balance between work hardening caused by dislocation entanglement and micro-softening caused by the formation of the slip bands. In contrast, the stress response behavior of the aged alloy is mainly dependent on the interaction between various precipitates with different types of dislocations. Compared with the T6-treated alloy, the T7-treated counterpart exhibits lower yield strength, higher ductility and more homogeneous deformation. The T6-treated alloy shows the initial cyclic hardening followed by cyclic softening mainly due to the retarding effect from the fine β'' precipitates on the dislocations-slip and the formation of the PSBs. For the T7-treated alloy, the large β_1 precipitates and the formation of PSBs during low cycle fatigue process

Figure 7 **a** Bright field image showing the slip bands and β'' precipitates in the T6-treated Mg–3.68 wt%Nd–0.58 wt%Zr alloy after 350 cycles; **b** bright field image showing the twins, β'' precipitates and β_1 precipitates after 350 cycles.

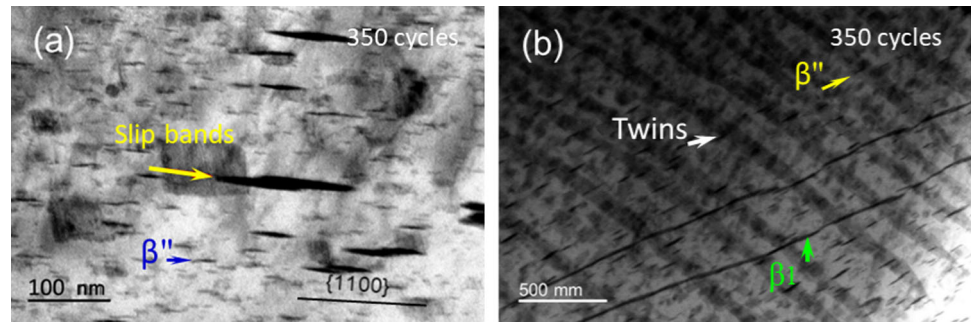
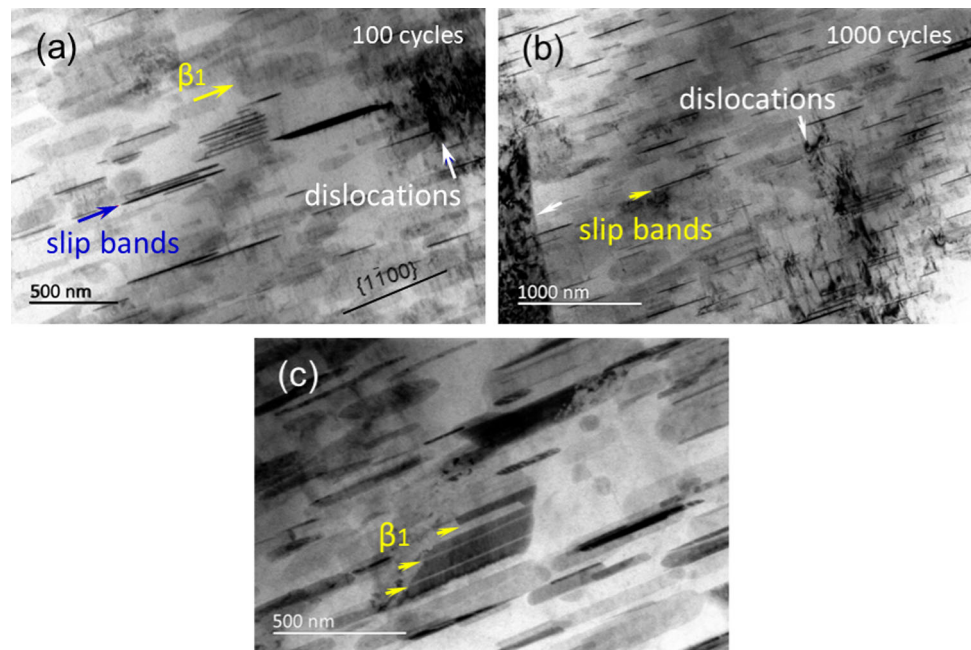


Figure 8 **a** Bright field image showing the dislocations and the slip bands in the T7-treated Mg–3.68 wt%Nd–0.58 wt%Zr alloy tested at total strain amplitude of 0.4% after 100 cycles ($B = [11\bar{2}0]_x$); **b** bright field image showing the microstructure of the T7-treated alloy after 1000 cycles; **c** bright field image showing the β_1 precipitates were cut by the dislocations.



led to lower cyclic stress amplitude and more homogeneous deformation.

Effect of grain size

TEM analysis results of the typical dislocation structures of the coarse-grained Mg–3.69 wt%Nd alloy (average grain size of $\sim 1625 \pm 236 \mu\text{m}$) tested at the total strain amplitude of 0.4% after 200 and 500 cycles are shown in Fig. 10 ($B = [11\bar{2}0]_x$). It is seen from Fig. 9a that large numbers of the dislocation bands (marked by yellow arrows) on the $(0001)_x$ basal plane and $\{1\bar{1}00\}_x$ prism plane were formed in the coarse-grained after 200 cycles. After 500 cycles, there are a series of complex interactions between dislocations in the coarse-grained, and a large number of the dislocations located on basal and non-basal planes (as shown in Fig. 9b) and dislocation entanglement (as shown in Fig. 9c) were formed. The increase of the

dislocation density and dislocation entanglement is the evidence of cyclic micro-hardening.

Figure 10 shows the typical dislocation distribution at the same location with different bass vectors in the T6-treated Mg–3.69Nd alloy after 1000 cycles. In the cases of $g = 0001$ and $g = 0002$, the dislocations in the matrix of the coarse-grained samples can be observed (as shown in Fig. 10a and b). The dislocations are considered to be $\langle a + c \rangle$ or $\langle c \rangle$ dislocations located on the $\{1\bar{1}00\}_x$ plane. Under the condition of $g = 1\bar{1}00$, the $\langle a \rangle$ dislocations located on basal and non-basal planes are still clearly visible (as shown in Fig. 10c). It is thus believed that for the T6-treated alloy with coarse-grains, both $\langle a \rangle$ dislocations and $\langle a + c \rangle$ or $\langle c \rangle$ dislocations located at the basal and non-basal planes participate in the plastic deformation. When the cyclic number is increased to 1000 cycles, some ring-shaped bands can be observed in the matrix of the coarse-grained alloy (as shown in

Figure 9 **a** Bright field image showing the dislocation morphology of the T6-treated Mg–3.69 wt%Nd alloy with coarser grains after 200 cycles ($B = [11\bar{2}0]_a$). **b** bright field image showing the typical dislocation distribution of the T6-treated Mg–3.69 wt%Nd alloy after 500 cycles [$B = (11 - 20)_a$]; **c** bright field image showing the dislocation entanglement in the matrix of the coarse-grained alloy [$B = (11 - 20)_a$].

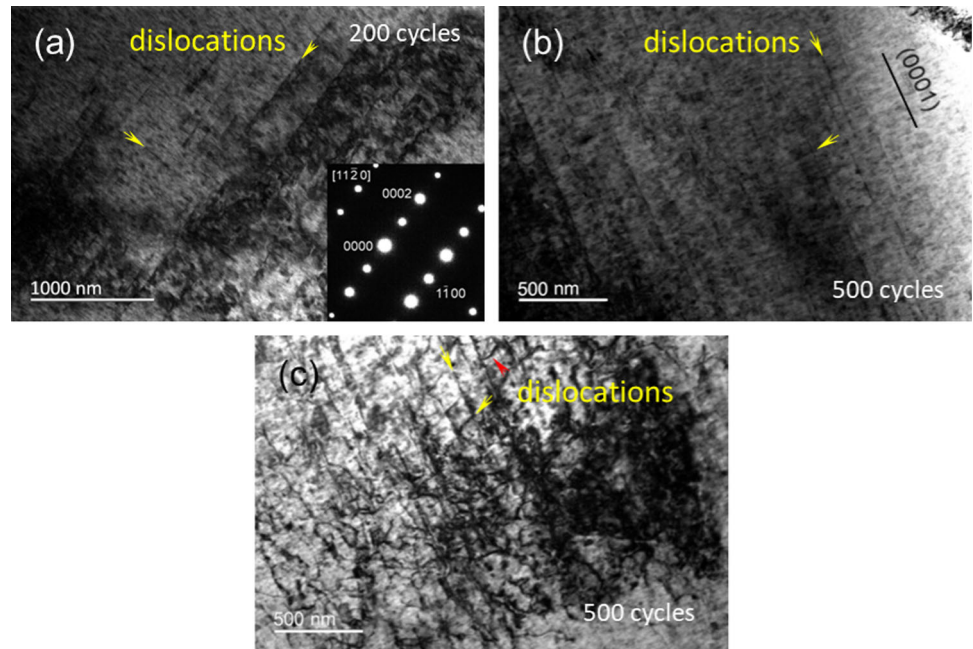


Figure 10 Bright field images showing the typical configuration of the dislocations in the T6-treated Mg–3.69 wt%Nd alloy at the same location after 1000 cycles: **a** $g = 0001$; **b** $g = 0002$; **c** $g = 1 - 100$ [$B = (11 - 20)_a$]; **d** bright field image showing some microscopic bands in the T6-treated alloy (after 1000 cycles).

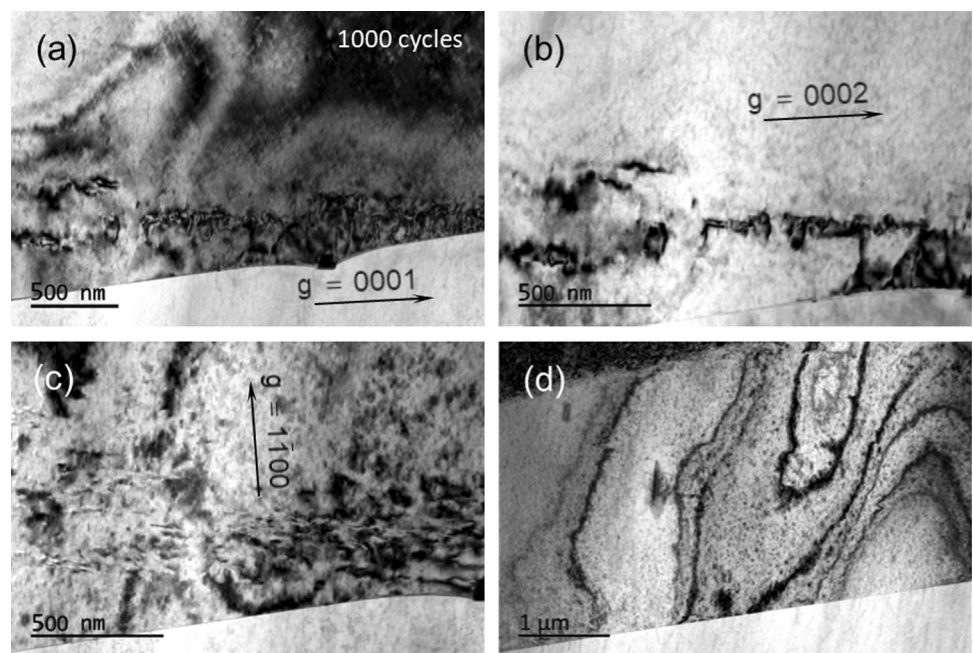


Fig. 10d). In terms of the morphology, the bands are similar to the dislocation bands, which are composed of the straight dislocations and bending dislocations. In contrast, no similar bands were observed in the fine-grained Mg–3.68Nd–0.58Zr–T6 alloy after 1000 cycles. Moreover, there is not enough evidence that the twins participate in the cyclic deformation. For the T6-treated Mg–3.69 wt%Nd alloy, therefore, the dislocations-slip located on basal and non-basal

planes is the main deformation mode. In addition, the evolution of the microstructure characteristic for the coarse-grained alloy is significantly different from that of the T6-treated Mg–3.68 wt%Nd–0.58 wt%Zr alloy during low cycle fatigue process. The precipitates of the coarse-grained alloy after 1000 cycles are also composed of large numbers of fine β'' precipitates.

For the fine-grained alloy, however, grain boundary is the main obstacle to dislocation movement besides the β'' precipitates in the initial stage of cyclic deformation. Similar to grain boundary, the twin boundary in the alloy with finer grains can also effectively block the movement of the dislocations [32, 48–50]. For the coarse-grained alloy, the effect of grain boundary can be ignored, and the existence of the β'' precipitates in the matrix has the most important impact on the dislocation movement and plastic deformation. In the region with low dislocation density, the matrix deforms forming high density dislocation entanglement. The high density dislocation region becomes a new obstacle to dislocation-slip, leading to cyclic micro-hardening. In addition, a variety of secondary interfaces are formed within grains through fatigue process in the alloy with coarser grains, which can further hinder the dislocation-slip.

For the fine-grained alloy, due to the blocking effect of grain boundary, the distance of the dislocations-slip is significantly shortened, and the probability of the dislocations cutting through precipitates and twins is significantly increased. In addition, the metastable β'' precipitates gradually transform into the β_1 and β precipitates because the activation of driving force provided by the stress concentration at the interface between β'' precipitates and matrix. The cyclic softening in the fine-grained alloy is mainly attributed to the transformation of the precipitates. Moreover, the formation of the micro-cracks particularly on the fatigued samples can also reduce the cyclic stress. In contrast, the coarse-grained alloy shows the longer free path of dislocation movement and lower hardening rate [51]. On the one hand, the dislocations cannot fully move to the grain boundary to coordinate the deformation, and the barrier effect of grain boundary can be ignored. On the other hand, the probability of the dislocation cutting through the precipitates is significantly reduced, and there is no precipitate phase transformation in the matrix of the coarse-grained alloy. At the late stage of fatigue, the cyclic softening for the coarsen-grained alloy is mainly due to the formation of the micro-cracks particularly on the fatigued samples. After the formation of cracks, the effective bearing area of the fatigue samples becomes smaller, and the permanent damage of the material is formed, thus reducing the response cyclic stress amplitude.

Conclusions

For the as-cast and the heat-treated Mg–3.68 wt%Nd–0.58 wt%Zr alloy with finer grains and the T6-treated Mg–3.69 wt%Nd alloy with coarser grains, different stress amplitude responses can be explained by the evolution of the microstructure and the competing mechanism between micro-hardening and micro-softening during the low-cycle fatigue.

- (1) Cyclic hardening in the T4-treated alloy is caused by dislocation entanglement. For the as-cast alloy, the work hardening from the dislocation density increment neutralizes the softening caused by micro-crack initiation, leading to cyclic stabilization after 500 cycles.
- (2) For the T6-treated alloy, both dislocation interaction and twinning participate in the plastic deformation of fatigue. The cyclic softening is mainly attributed to the precipitate transformation from β'' to β_1 and β and the coarsening of β_1 precipitates in the fine-grained alloy. For the T7-treated alloy, there is a balance between work hardening and stress release due to the formation of slip bands. In the microstructure with coarse grains, only dislocation-slip mechanism is involved in the fatigue deformation.
- (3) Dislocation shearing is the key factor in the precipitate phase transition of the fine-grained alloy. The short slip distance in the studied alloy with fine grains increases the probability of dislocation cutting through precipitates and twins.

Acknowledgements

This work was supported by the Key Research and Development Plan Projects of Zhejiang Province (No. 2021C01139). The authors would also like to thank Dr. H. Zhou of Nanjing University of Science and Technology for providing his assistance in TEM observation. The authors are grateful to Dr. Qigui Wang (General Motors) and Prof. Liming Peng (Shanghai Jiaotong University) for his helpful discussions.

Author contributions

PZ completed the fatigue tests and TEM analysis and manuscript writing. Z has given a lot of guidance in the process of testing experiments, the analysis results of TEM (especially for the dislocation-slip and twin) and manuscript writing.

Data availability

The datasets used and/or analyzed during the current study are available from the corresponding author on reasonable.

Code availability

The datasets used and/or analyzed during the current study are available from the corresponding author on reasonable.

Declarations

Conflicts of interest The authors declare that they have no known competing financial interests or personal relationships that could have appeared to influence the work reported in this paper.

References

- [1] Liu ZH, Han EH, Liu L (2008) High-cycle fatigue behavior of Mg–Zn–Y–Zr alloy. *Mater Sci Eng A* 483–484:373–375. <https://doi.org/10.1016/j.msea.2006.08.135>
- [2] Mirza FA, Chen DL, Li DJ, Zeng XQ (2015) Cyclic deformation behavior of a rare-earth containing extruded magnesium alloy: effect of heat treatment. *Metall Mater Trans A* 46:1168–1187. <https://doi.org/10.1007/s11661-014-2687-1>
- [3] Li ZM, Wang QG, Luo AA, Peng LM, Fu PH, Wang YX (2013) Improved high cycle fatigue properties of a new magnesium alloy. *Mater Sci Eng A* 582:170–177. <https://doi.org/10.1016/j.msea.2013.06.001>
- [4] Zhu R, Ji WQ, Wu YJ, Cai XT, Yu Y (2012) Effect of aging treatment on low-cycle fatigue behavior of extruded Mg–8Al–0.5Zn alloys. *Mater Des* 41:203–207. <https://doi.org/10.1016/j.matdes.2012.05.015>
- [5] Li HZ, Lv F, Xiao ZY, Liang XP, Sang FJ, Li PW (2016) Low-cycle fatigue behavior of a cast Mg–Y–Nd–Zr alloy by T6 heat treatment. *Mater Sci Eng A* 676:377–384. <https://doi.org/10.1016/j.msea.2016.09.001>
- [6] Rettberg LH, Jordon JB, Horstemeyer MF, Jones JW (2012) Low-cycle fatigue behavior of die-cast Mg alloys AZ91 and AM60. *Metall Mater Trans A* 43:2260–2274. <https://doi.org/10.1007/s11661-012-1114-8>
- [7] Liu WC, Wu GH, Zhai CQ, Ding WJ, Korsunsky AM (2013) Grain refinement and fatigue strengthening mechanisms in as-extruded Mg–6Zn–0.5Zr and Mg–10Gd–3Y–0.5Zr magnesium alloys by shot peening. *Int J Plasticity* 49:16–35. <https://doi.org/10.1016/j.ijplas.2013.02.015>
- [8] Dong J, Liu WC, Song X, Zhang P, Ding WJ, Korsunsky AM (2010) Influence of heat treatment on fatigue behavior of high-strength Mg–10Gd–3Y alloy. *Mater Sci Eng A* 527:6053–6063. <https://doi.org/10.1016/j.msea.2010.06.030>
- [9] Li ZM, Wang QG, Luo AA, Dai JC, Zou H, Peng LM (2018) Effect of heat treatment on strain-controlled fatigue behavior of cast Mg–Nd–Zn–Zr alloy. *J Mater Sci Technol* 11:2091–2099. <https://doi.org/10.1016/j.jmst.2018.05.001>
- [10] Li ZM, Luo AA, Wang QG, Peng LM, Zhang P (2016) Fatigue properties of cast magnesium wheels. *Metall Mater Trans A* 47:4239–4257. <https://doi.org/10.1007/s11661-016-3550-3>
- [11] Fu PH, Peng LM, Jiang HY, Chang JW, Zhai CQ (2008) Effects of heat treatments on the microstructures and mechanical properties of Mg–3Nd–0.2Zn–0.4Zr (wt.%) alloy. *Mater Sci Eng A* 486:183–192. <https://doi.org/10.1016/j.msea.2007.08.064>
- [12] Nie JF (2012) Precipitation and hardening in magnesium alloys. *Metall Mater Trans A* 43A:3891–3939. <https://doi.org/10.1007/s11661-012-1217-2>
- [13] Li ZM, Wang QG, Luo AA, Zhang P, Peng LM (2016) Size effect on magnesium alloy castings. *Metall Mater Trans A* 47A:2686–2704. <https://doi.org/10.1007/s11661-016-3436-4>
- [14] Mirza FA, Chen DL, Li DJ, Zeng XQ (2014) Low cycle fatigue of an extruded Mg–3Nd–0.2Zn–0.5Zr magnesium alloy. *Mater Des* 64:63–73. <https://doi.org/10.1016/j.matdes.2014.07.016>
- [15] Wang FH, Dong J, Jiang YY, Ding WJ (2013) Cyclic deformation and fatigue of extruded Mg–Gd–Y magnesium alloy. *Mater Sci Eng A* 561:403–410. <https://doi.org/10.1016/j.msea.2012.10.048>
- [16] Zhu R, Cai XT, Wu YJ, Liu LL, Ji WQ, Hua B (2014) Low-cycle fatigue behavior of extruded Mg–10Gd–2Y–0.5Zr alloys. *Mater Des* 53:992–997. <https://doi.org/10.1016/j.matdes.2013.07.099>
- [17] Yin SM, Li SX (2013) Low-cycle fatigue behaviors of an As-extruded Mg–12%Gd–3%Y–0.5%Zr alloy. *J Mater Sci Technol* 29:775–780. <https://doi.org/10.1016/j.jmst.2013.04.011>
- [18] Bahadur F, Biswas K, Gurao NP (2020) Micro-mechanisms of microstructural damage due to low cycle fatigue in

- CoCuFeMnNi high entropy alloy. *Int J Fatigue* 130:105258. <https://doi.org/10.1016/j.ijfatigue.2019.105258>
- [19] Li PW, Li HZ, Liang XP, Che YX, Zhan X, Huang L (2018) Effect of isothermal and non-isothermal aging on the low cycle fatigue behavior of an Al–Cu–Mg–Si forging alloy. *Mater Charact* 144:378–386. <https://doi.org/10.1016/j.matchar.2018.07.027>
- [20] Wu LY, Yang Z, Xia WJ, Chen ZH, Yang L (2012) The cyclic softening and evolution of microstructures for Mg–10Gd–2.0Y–0.46Zr alloy under low cycle fatigue at 573 K. *Mater Des* 36:47–53. <https://doi.org/10.1016/j.matdes.2011.10.056>
- [21] Watanabe C, Jin CY, Monzen R, Kitagawa K (2004) Low-cycle fatigue behavior and dislocation structure of an Al–Mg–Sc alloy. *Mater Sci Eng A* 387–389:552–555. <https://doi.org/10.1016/j.msea.2004.05.079>
- [22] Begum S, Chen DL, Xu S, Luo AA (2009) Low cycle fatigue properties of an extruded AZ31 magnesium alloy. *Int J Fatigue* 31:726–735. <https://doi.org/10.1016/j.ijfatigue.2008.03.009>
- [23] Wu L, Agnew SR, Brown DW, Stoica GM, Clausen B, Jain A, Fielden DE, Liaw PK (2008) Internal stress relaxation and load redistribution during the twinning–detwinning-dominated cyclic deformation of a wrought magnesium alloy, ZK60A. *Acta Mater* 56:688–695. <https://doi.org/10.1016/j.actamat.2008.04.006>
- [24] Zhang MJ, Zhang H, Ma AX, Llorca J (2021) Experimental and numerical analysis of cyclic deformation and fatigue behavior of a Mg–RE alloy. *Int J Plasticity* 139:102885. <https://doi.org/10.1016/j.ijplas.2020.102885>
- [25] Xie D, Lyu ZY, Li Y, Liaw PK, Chew HB, Ren Y, An K, Gao YF (2021) In situ monitoring of dislocation, twinning, and detwinning modes in an extruded magnesium alloy under cyclic loading conditions. *Mater Sci Eng A* 806:140860. <https://doi.org/10.1016/j.msea.2021.140860>
- [26] Li ZM, Wang QG, Luo AA, Fu PH, Peng LM, Wang YX, Wu GH (2013) High cycle fatigue of cast Mg–3Nd–0.2Zn magnesium alloys. *Metal Mater Trans A* 44A:5202–5215. <https://doi.org/10.1007/s11661-013-1843-3>
- [27] Rho BS, Hong HU, Nam SW (1998) The fatigue crack initiation at the interface between matrix and δ -ferrite in 304L stainless steel. *Scr Mater* 39:1407–1412. [https://doi.org/10.1016/S1359-6462\(98\)00327-3](https://doi.org/10.1016/S1359-6462(98)00327-3)
- [28] Liu HB, Yang SL, Xie CJ, Zhang Q, Cao YM (2018) Mechanisms of fatigue crack initiation and propagation in 6005A CMT welded joint. *J Alloys Comp* 741:188–196. <https://doi.org/10.1016/j.jallcom.2017.12.374>
- [29] Sangid MD, Maier JJ, Sehitoglu HY (2011) A physically based fatigue model for prediction of crack initiation from persistent slip bands in polycrystals. *Acta Mater* 59:328–341. <https://doi.org/10.1016/j.actamat.2010.09.036>
- [30] Bhattacharyya JJ, Wang F, Stanford N (2018) Slip mode dependency of dislocation shearing and looping of precipitates in mg alloy WE43. *Acta Mater* 146:55–62. <https://doi.org/10.1016/j.actamat.2017.12.043>
- [31] Fu PH, Peng LM, Nie JF, Jiang HY, Ma L, Bourgeois L (2011) Ductility improvement of Mg–Nd–Zr cast alloy by trace addition of Zn. *Mater Sci Forum* 690:230–233. <https://doi.org/10.4028/www.scientific.net/MSF.690.230>
- [32] Li ZM, Wang QG, Peng LM, Luo AA, Fu PH (2022) Low-cycle fatigue behavior of peak-aged Mg–Nd-based alloy. *Metall Mater Trans A* 53:754–761. <https://doi.org/10.1007/s11661-021-06465-5>
- [33] Zhu YT, Wu XL, Liao XZ, Narayan J, Kecskés LJ, Mathaudhu SN (2011) Dislocation-twin interactions in nanocrystalline fcc metals. *Acta Mater* 59:812–821. <https://doi.org/10.1016/j.actamat.2010.10.028>
- [34] Reinholz B, Brinckmann S (2012) Phase transformations in the proximity of TiC precipitates in NiTi matrix during fatigue. *Int J Fatigue* 41:72–82. <https://doi.org/10.1016/j.ijfatigue.2012.01.017>
- [35] König D, Zarnetta R, Savan A, Brunken H, Ludwig A (2011) Phase transformation, structural and functional fatigue properties of Ti–Ni–Hf shape memory thin films. *Acta Mater* 59:3267–3275. <https://doi.org/10.1016/j.actamat.2011.01.066>
- [36] Chan KS (2021) Mechanistic modeling of cyclic softening and slip localization in Ni-based superalloys. *Metall Mater Trans A* 52:1759–1776. <https://doi.org/10.1007/s11661-021-06187-8>
- [37] Clinard FW, Sherby OD (1964) Strength of Iron during allotropic transformation. *Acta Metall* 12:911–999. [https://doi.org/10.1016/0001-6160\(64\)90151-8](https://doi.org/10.1016/0001-6160(64)90151-8)
- [38] Li J, Fang QH, Liu B, Liu Y (2018) Transformation induced softening and plasticity in high entropy alloys. *Acta Mater* 147:35–41. <https://doi.org/10.1016/j.actamat.2018.01.002>
- [39] Ji XK, Guo BQ, Jiang FL, Yu H, Fu DF, Teng J, Zhang H, Jonas JJ (2020) Accelerated flow softening and dynamic transformation of Ti–6Al–4V alloy in two-phase region during hot deformation via coarsening α grain. *J Mater Sci Technol* 36:160–166. <https://doi.org/10.1016/j.jmst.2019.08.005>
- [40] Xiao L, Chen DL, Chaturvedi MC (2005) Shearing of γ'' precipitates and formation of planar slip bands in Inconel 718 during cyclic deformation. *Scr Mater* 52:603–607. <https://doi.org/10.1016/j.scriptamat.2004.11.023>
- [41] Alizadeh R, Llorca J (2020) Interactions between basal dislocations and β'_1 precipitates in Mg–4Zn alloy:

- mechanisms and strengthening. *Acta Mater* 186:475–486. <https://doi.org/10.1016/j.actamat.2020.01.028>
- [42] Huang ZH, Yang CM, Allison JE, Qi L, Misra A (2021) Dislocation cross-slip in precipitation hardened Mg–Nd alloys. *J Alloys Comp* 859:157858. <https://doi.org/10.1016/j.jallcom.2020.157858>
- [43] Lee SW, Kim SH, Jo WK, Hong WH, Kim W, Moon BG, Park SH (2019) Twinning and slip behaviors and microstructural evolutions of extruded Mg–1Gd alloy with rare-earth texture during tensile deformation. *J Alloy Comp* 791:700–710. <https://doi.org/10.1016/j.jallcom.2019.03.316>
- [44] Yin DD, Boehlert CJ, Long LJ, Huang GH, Zhou H, Zheng J, Wang QD (2021) Tension-compression asymmetry and the underlying slip/twinning activity in extruded Mg–Y sheets. *Int J Plast* 136:102878. <https://doi.org/10.1016/j.ijplas.2020.102878>
- [45] Deng YC, Huang ZJ, Li TJ, Yin DD, Zheng J (2021) Quantitative investigation on the slip/twinning activity and cracking behavior during low-cycle fatigue of an extruded Mg–3Y sheet. *Metall Mater Trans A* 52:332–349. <https://doi.org/10.1007/s11661-020-06083-7>
- [46] Feaugas X, Clavel M (1997) Cyclic deformation behaviour of an α/β titanium alloy-I. Micromechanisms of plasticity under various loading paths. *Acta Mater* 45:2685–2701. [https://doi.org/10.1016/S1359-6454\(96\)00406-5](https://doi.org/10.1016/S1359-6454(96)00406-5)
- [47] Watanabe C, Jin CY, Monzen R (2004) Low-cycle fatigue behavior and dislocation structure of an Al–Mg–Sc alloy. *Mater Sci Eng A* 387(1):552–555. <https://doi.org/10.1016/j.msea.2004.05.079>
- [48] Su HH, Zhou XZ, Zheng SJ, Ye HQ, Yang ZQ (2021) Atomic-resolution studies on reactions between basal dislocations and 10–12 coherent twin boundaries in a Mg alloy. *J Mater Sci Technol* 66:28–35. <https://doi.org/10.1016/j.jmst.2020.06.017>
- [49] Li N, Wang J, Misra A, Zhang X, Huang JY, Hirth JP (2011) Twinning dislocation multiplication at a coherent twin boundary. *Acta Mater* 59:5989–5996. <https://doi.org/10.1016/j.actamat.2011.06.007>
- [50] Xu J, Guan B, Yu HH, Cao XZ, Xin YC, Liu Q (2016) Effect of twin boundary–dislocation–solute interaction on detwinning in a Mg–3Al–1Zn alloy. *J Mater Sci Technol* 32(12):1239–1244. <https://doi.org/10.1016/j.jmst.2016.08.023>
- [51] Wang QG, Cáceres CH (1998) The fracture mode in Al–Si–Mg casting alloys. *Mater Sci Eng A* 241:72–82. [https://doi.org/10.1016/S0921-5093\(97\)00476-0](https://doi.org/10.1016/S0921-5093(97)00476-0)

Publisher's Note Springer Nature remains neutral with regard to jurisdictional claims in published maps and institutional affiliations.

Springer Nature or its licensor (e.g. a society or other partner) holds exclusive rights to this article under a publishing agreement with the author(s) or other rightsholder(s); author self-archiving of the accepted manuscript version of this article is solely governed by the terms of such publishing agreement and applicable law.